

ORIGINAL ARTICLE

Open Access



Impact Force Localization and Reconstruction via ADMM-based Sparse Regularization Method

Yanan Wang^{1,2}, Lin Chen^{1,2}, Junjiang Liu^{1,2}, Baijie Qiao^{1,2*}, Weifeng He^{1,2} and Xuefeng Chen^{1,2}

Abstract

In practice, simultaneous impact localization and time history reconstruction can hardly be achieved, due to the ill-posed and under-determined problems induced by the constrained and harsh measuring conditions. Although ℓ_1 regularization can be used to obtain sparse solutions, it tends to underestimate solution amplitudes as a biased estimator. To address this issue, a novel impact force identification method with ℓ_p regularization is proposed in this paper, using the alternating direction method of multipliers (ADMM). By decomposing the complex primal problem into sub-problems solvable in parallel via proximal operators, ADMM can address the challenge effectively. To mitigate the sensitivity to regularization parameters, an adaptive regularization parameter is derived based on the K -sparsity strategy. Then, an ADMM-based sparse regularization method is developed, which is capable of handling ℓ_p regularization with arbitrary p values using adaptively-updated parameters. The effectiveness and performance of the proposed method are validated on an aircraft skin-like composite structure. Additionally, an investigation into the optimal p value for achieving high-accuracy solutions via ℓ_p regularization is conducted. It turns out that $\ell_{0.6}$ regularization consistently yields sparser and more accurate solutions for impact force identification compared to the classic ℓ_1 regularization method. The impact force identification method proposed in this paper can simultaneously reconstruct impact time history with high accuracy and accurately localize the impact using an under-determined sensor configuration.

Keywords Impact force identification, Non-convex sparse regularization, Alternating direction method of multipliers, Proximal operators

1 Introduction

Characterized by exceptional properties of high strength-to-weight ratio, composites have been widely used in such industries as the aerospace to make transportation lighter [1]. Unfortunately, composite structures are quite sensitive to impact forces from foreign object debris (FOD) like stones, hail and birds during service, and are

then susceptible to the barely visible impact damage (BVID), including delamination and debonding [2, 3]. Such internal damage is tricky to be detected by the routine procedure like preflight visual inspection, and can wherefore wreak havoc on structural integrity, jeopardizing service security and even cause catastrophic failure [4]. To detect the damage at an early stage, impact force monitoring has received considerable attention for its progress in reducing human interference and decreasing maintenance cost [5]. It is of great help for monitoring the safety and integrity of composite structures to know and record the impact event such as its time history and location [2]. Measuring impact forces directly with transducers tends to be impractical, considering

*Correspondence:

Baijie Qiao
qiao1224@xjtu.edu.cn

¹ National Key Lab of Aerospace Power System and Plasma Technology, Xi'an Jiaotong University, Xi'an 710049, China

² School of Mechanical Engineering, Xi'an Jiaotong University, Xi'an 710049, China



© The Author(s) 2024. **Open Access** This article is licensed under a Creative Commons Attribution 4.0 International License, which permits use, sharing, adaptation, distribution and reproduction in any medium or format, as long as you give appropriate credit to the original author(s) and the source, provide a link to the Creative Commons licence, and indicate if changes were made. The images or other third party material in this article are included in the article's Creative Commons licence, unless indicated otherwise in a credit line to the material. If material is not included in the article's Creative Commons licence and your intended use is not permitted by statutory regulation or exceeds the permitted use, you will need to obtain permission directly from the copyright holder. To view a copy of this licence, visit <http://creativecommons.org/licenses/by/4.0/>.

that the excitation sources may be unknown or the excitation location may not be available for the transducer installation. In consequence, an indirect alternative that has come into the spotlight these days is impact force identification (IFI) technique, which combines together the accessible responses collected by easy-to-use sensors like strain gages and the dynamic model of the monitored structure. However, participate to solve the impact forces in this inverse problem accurately, tailored algorithms are required.

Normally, IFI incorporates two main tasks including force history reconstruction and impact localization [6, 7]. Jacquelin et al. [8] employed truncated singular value decomposition (TSVD) and Tikhonov regularization (TR) to reconstruct impact forces in time domain respectively for a comparative study. Thite et al. [9] conducted the force reconstruction through a plate simulation study in frequency domain using TSVD, and proposed a singular value rejection threshold criterion. Tran et al. [10] developed a deconvolution technique for impact force reconstruction in wavelet domain based on TSVD. Zhang et al. [11] presented a Bayesian regularization (BR) approach for force reconstruction to cope with an uncertain structural model, jointly using Monte Carlo Markov chain to determine the unknown forces. Li et al. [12] dealt with the force identification problem via BR in conjunction with adaptive ℓ_q ($q = 1$ or 2) norm, treating force history, precision parameters and q as random unknowns. When it comes to IFI, TSVD, TR and BR often cannot produce the force history with high accuracy generally, since they penalize solutions smoothly and false forces appear at unloading stage.

In composite structural health monitoring, localization is often considered as the first step in quickly measuring impact forces to avoid fatal damage to the structure. Qiu et al. [13] employed pattern recognition to localize the impact firstly in time domain and then reconstructed its history using the TR method. Yan et al. [14] presented a two-step method to accomplish the IFI of the composite plate, localizing the impact using a nonlinear unscented Kalman filter first and then reconstructing impact force time history by BR. When the number of monitored locations rises, accessible measurements are limited and under-determined cases might be faced. Traditional methods are usually incapable of dealing with these problems, especially for identifying time history and localization simultaneously [15]. As an eye-catching regularization method, sparse regularization (SR) explores the inherent sparsity of impact forces in the joint time-space domain [16–18], making it very popular in fields such as fault diagnosis [19, 20] and image processing [21]. Under such strong constraints brought by sparse priors, SR can achieve the force reconstruction and impact

localization at the same time, even in under-determined circumstances [22]. Ginsberg et al. [17] addressed IFI via SR, and achieves simultaneous localization and reconstruction of the impact force with a basis pursuit denoising algorithm. Also other types of loads, say, moving forces [23] and distributed forces [24] are able to be identified by SR. To further promote the identification accuracy, enhanced SR [25] and group SR [16, 26] were proposed respectively.

These aforementioned methods are ℓ_1 -norm based SR, as a relaxation of ℓ_0 -norm, which unavoidably produce biased estimations and underestimate the true solution [27–29]. Then non-convex penalties are getting more and more attention in place of ℓ_1 -norm to improve the sparsity and accuracy of IFI [22, 30–32]. As a typical non-convex regularizer, the quasi-norm ℓ_p ($0 \leq p < 1$) has gained popularity in a wide range of fields [27, 28] because the non-convex ℓ_p regularization performs much better than the convex ℓ_1 regularization in promoting sparsity and obtaining more accurate solutions when $p < 1$. Several typical algorithms have been employed to resolve ℓ_p -norm regularized IFI problems. Aucejo [31] introduced an iteratively reweighted least-squares (IRLS) algorithm to solve the multi-parameter multiplicative ℓ_p regularization model of IFI in frequency domain. Qiao [32] adopted an iteratively reweighted ℓ_1 -norm (IRL1) algorithm to tackle an additive ℓ_p regularization regularized IFI model in time domain. Both IRLS and IRL1 suffer from several limitations when implemented in IFI: (i) The two algorithms optimize the surrogate functions respectively rather than the original function, so the solution accuracy is limited [33]; (ii) These two algorithms converge to an undesired local minima when an inappropriate initial solution is utilized, so pre-computing the initial solution is generally required, which is time-consuming and unstable [31, 32]; (iii) Both algorithms usually admit slow convergence when the transfer matrix is ill-conditioned [33]. Thus, the non-convex ℓ_p optimization problem still remains difficult for IFI.

In this contribution, in order to address the aforesaid issues existing in ℓ_p regularization, a novel ℓ_p sparse regularization approach for IFI is proposed based on the principle of ADMM [34], which can simultaneously reconstruct force time-history and localize the impact with an under-determined sensor configuration. The proposed ADMM-based algorithm for IFI shows the following merits: (i) By virtue of ADMM, the primal complicated problem is split into three easier sub-problems, so the large-scale problems caused by multi-point impact monitoring can be solved; (ii) Each subproblem is resolved directly in virtue of proximal operators, which can promote high-accuracy IFI results; (iii) This algorithm ensures that it converges to a stationary point,

providing feasible solutions for IFI; (iv) The non-convex optimization requires no well-chosen initial solution in advance; (v) The algorithm solves non-convex sparse regularization problems with arbitrary p values. Nonetheless, the solutions produced by regularization technique are considerably sensitive to the regularization parameter, and inappropriate choices result in poor estimations. Unfortunately, there is still no versatile criteria for regularization parameter selection [35]. In this article, an adaptive parameter strategy is proposed for IFI: (i) The IFI problem is translated into a K -sparsity problem by considering the joint space-time sparsity priori; (ii) An adaptive regularization parameter is derived according to the relationship between the sparsity value K and the regularization parameter λ ; (iii) The optimal sparsity value K is determined by minimizing the identification mean squared error (MSE) which is feasibly estimated by Monte Carlo Generalized Stein Unbiased Risk Estimate (MC-GSURE) technique [36]; (iv) Once K is decided, an adaptive λ is automatically updated at each iteration and fine-tuning is not required even if the noise level of measurements changes. Finally, an ADMM-based Sparse Regularization method named **ADMM-SpaRe** is proposed for IFI.

This paper is organized in the following way. In Section 2, inverse analysis for impact force reconstruction and localization is presented as the theoretical background. In Section 3, the ℓ_p sparse regularization model for IFI is established, an efficient algorithm termed ADMM-SpaRe is proposed to resolve this model, and parameter setting strategies are discussed in detail. Section 4 presents a series of experimental studies to prove the effectiveness and performance of the proposed method and compares the results of this method with those of the ℓ_0 and ℓ_1 regularization methods. The conclusions are summarized in Section 5.

2 Inverse Analysis for Impact Force reconstruction and Localization

For a linear time-invariant (LTI) multi-input/multi-output (MIMO) mechanical system, when subjected to impact forces, its structural responses can be obtained via the convolution integral as

$$x_i(t) = \sum_{j=1}^{n_f} \int_0^t f_j(\tau) h_{ij}(t - \tau) d\tau, \tag{1}$$

where $x_i(t)$ represents the response at point i , and the impulse response function (IRF) $h_{ij}(t)$ denotes the linear transmission between the external force at the input position j ($j \in \{1, 2, \dots, n_f\}$) and the response at the output position i ($i \in \{1, 2, \dots, n_r\}$) in continuous

time domain. Zero initial conditions are assumed, i.e., $f_j(t) = h_{ij}(t) = x_i(t) = 0$ when $t < 0$ are assumed. Discretizing the convolution integral with a fixed sampling interval Δt leads to the following algebraic equation [17, 37],

$$\mathbf{x}_i = \sum_{j=1}^{n_f} \mathbf{H}_{ij} \mathbf{f}_j, \tag{2}$$

in which $\mathbf{H}_{ij} \in \mathbb{R}^{N \times N}$ is a Toeplitz-like matrix and N is the analyzed data length. Eq. (2) can be rewritten in matrix-vector form as,

$$\mathbf{x}_i = [\mathbf{H}_{i1} \ \mathbf{H}_{i2} \ \dots \ \mathbf{H}_{in_f}] \mathbf{f}, \tag{3}$$

where $\mathbf{f} = [\mathbf{f}_1 \ \mathbf{f}_2 \ \dots \ \mathbf{f}_{n_f}]^T \in \mathbb{R}^{n_f \times N}$. For a MIMO dynamic system, a more generalized form of Eq. (3) can be expressed as,

$$\begin{bmatrix} \mathbf{x}_1 \\ \mathbf{x}_2 \\ \vdots \\ \mathbf{x}_{n_r} \end{bmatrix} = \begin{bmatrix} \mathbf{H}_{11} & \mathbf{H}_{12} & \dots & \mathbf{H}_{1n_f} \\ \mathbf{H}_{21} & \mathbf{H}_{22} & \dots & \mathbf{H}_{2n_f} \\ \vdots & \vdots & \ddots & \vdots \\ \mathbf{H}_{n_r1} & \mathbf{H}_{n_r2} & \dots & \mathbf{H}_{n_rn_f} \end{bmatrix} \begin{bmatrix} \mathbf{f}_1 \\ \mathbf{f}_2 \\ \vdots \\ \mathbf{f}_{n_f} \end{bmatrix}. \tag{4}$$

Then, a compact output form for impact responses can be written as,

$$\mathbf{x} = \mathbf{H} \mathbf{f} \tag{5}$$

with the transfer matrix $\mathbf{H} \in \mathbb{R}^{n_r \cdot N \times n_f \cdot N}$, the impact force vector $\mathbf{f} \in \mathbb{R}^{n_f \cdot N}$ and the measurement vector $\mathbf{x} \in \mathbb{R}^{n_r \cdot N}$. Once \mathbf{f} is obtained, both the time history and localization of impact forces are known.

As for the forward problem, once the transfer matrix \mathbf{H} and the external force vector \mathbf{f} are known, responses \mathbf{x} can be readily calculated using Eq. (5). When the transfer matrix \mathbf{H} and responses of the mechanical system are known to monitor the external impact forces acting on it, namely solving \mathbf{f} in Eq. (5), the inverse problem is termed impact force identification (IFI). Generally, according to the relationship between the quantity of inputs and outputs, IFI problems are divided into three categories: 1) the over-determined case when $n_r > n_f$; 2) the even-determined case when $n_r = n_f$; 3) the under-determined case when $n_r < n_f$. Whatever the case, IFI may be intrinsically ill-conditioned, for even minute variations can cause large fluctuations in force identification. Furthermore, this inverse problem might be ill-posed, as the use of noisy and limited measurements cannot consequentially produce a unique and stable solution, especially in the under-determined case, and tackling the under-determined case is the focus of this work.

Inevitably, noise is introduced into the measurements causing the solution to "runs away" uncontrollably, and it

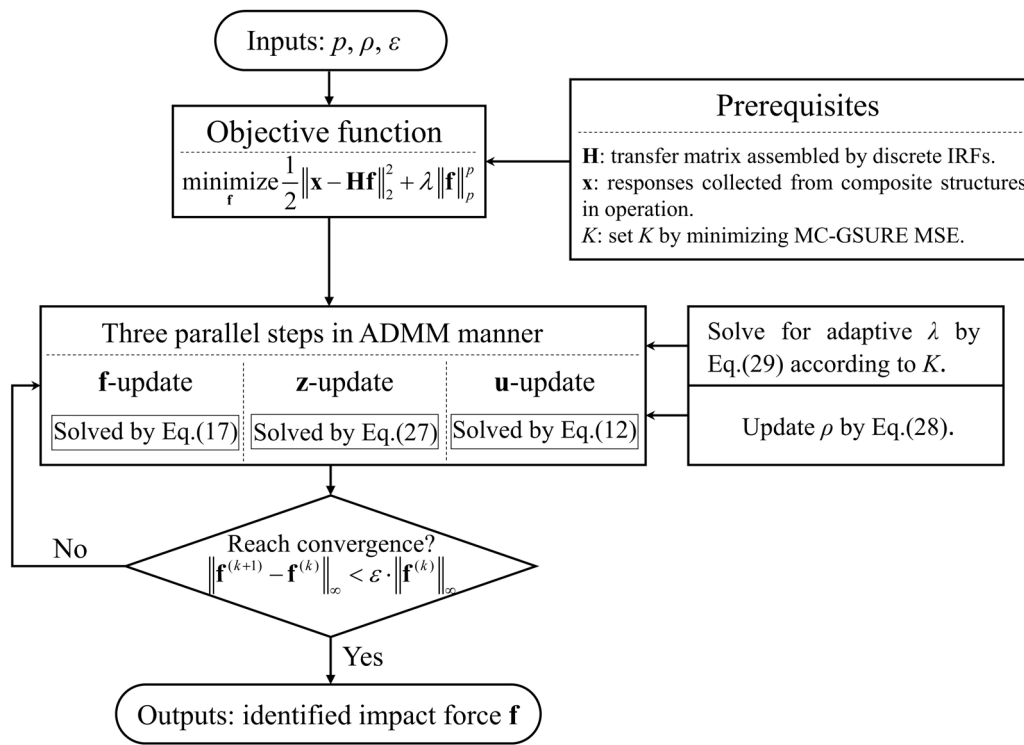


Figure 1 A brief flowchart of ADMM-SpaRe for IFI

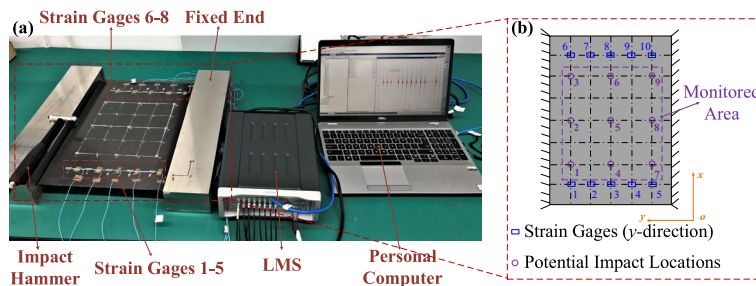


Figure 2 Experimental set-up of the composite laminated plate test: (a) Measurement setup, (b) Sensor placement

is hardly possible to obtain the desired result through classical methods, like QR factorization or least squares. But it is the stable and unique solution that allows for a meaningful interpretation in relation to the basic inverse problem model. Thus, the impact force identification problem is reformulated by numerical treatment. The well-known regularization technique is resorted to, containing additional assumptions of the solution like sparsity. In this work, an ADMM-based ℓ_p sparse regularization method with adaptive regularization parameters is proposed for IFI in the under-determined case.

3 Formulation of IFI via ℓ_p Regularization

To stabilize the resolving of Eq. (5) for \mathbf{f} , since the inverse problem may be ill-conditioned or ill-posed (e.g., the condition number of \mathbf{H} is quite large or \mathbf{H} is singular), the ℓ_p regularization technique is brought in,

$$\text{minimize}_{\mathbf{f}} \frac{1}{2} \|\mathbf{x} - \mathbf{H}\mathbf{f}\|_2^2 + \lambda \|\mathbf{f}\|_p^p, \tag{6}$$

where the first term $\frac{1}{2} \|\mathbf{x} - \mathbf{H}\mathbf{f}\|_2^2$ measures the differences between the linear model $\mathbf{H}\mathbf{f}$ and the output \mathbf{x} , the second term $\|\mathbf{f}\|_p^p$ measures the sparsity of \mathbf{f} , and the positive constant λ is the so-called regularization parameter. When $p = 2$, this model is known as the Tikhonov

regularization and is one of the most widely employed models for regularization of linear inverse problems. When $p = 1$, the model is called the least absolute shrinkage and selection operator(LASSO). Here, the ℓ_p -norm ($0 < p \leq 1$) is defined loosely,

$$\|\mathbf{f}\|_p = (|f_1|^p + |f_2|^p + \dots + |f_n|^p)^{1/p}. \quad (7)$$

Additionally, when $p = 0$, the ℓ_0 -norm defines that $\|\mathbf{f}\|_0$ is the quantity of non-zero entries of \mathbf{f} . These quasi-norms have been extensively applied in many fields thanks to their excellent properties [27, 28, 38].

The regularization method based on ℓ_p -norm is hard to be optimized. Especially, the resulting optimization problem is not convex while $0 \leq p < 1$. The non-convex problem is usually intractable as undesired local minima tend to be acquired reluctantly. To deal with the ℓ_p regularization model for IFI, an efficient algorithm is developed under ADMM framework.

3.1 Reformulating the IFI Model under ADMM Principle

As one of splitting methods, ADMM is a simple but powerful optimization algorithm that works for both convex and non-convex problems [34]. By means of ADMM, the problem (6) can be reformulated as,

$$\underset{\mathbf{f}}{\text{minimize}} F(\mathbf{f}) + G(\mathbf{z}), \quad \text{subject to } \mathbf{f} - \mathbf{z} = \mathbf{0}, \quad (8)$$

where the data fidelity term $F(\mathbf{f}) = \frac{1}{2} \|\mathbf{x} - \mathbf{H}\mathbf{f}\|_2^2$, the penalty term $G(\mathbf{z}) = \lambda \|\mathbf{z}\|_p^p$, and an additional vector of variable \mathbf{z} is introduced for variable splitting. Then, the augmented Lagrangian can be derived as [34],

$$L_\rho(\mathbf{f}, \mathbf{z}, \mathbf{u}) = \frac{1}{2} \|\mathbf{x} - \mathbf{H}\mathbf{f}\|_2^2 + \lambda \|\mathbf{z}\|_p^p + \rho \mathbf{u}^T (\mathbf{f} - \mathbf{z}) + \frac{\rho}{2} \|\mathbf{f} - \mathbf{z}\|_2^2, \quad (9)$$

where \mathbf{u} is a scaled vector of Lagrangian multipliers, and ρ denotes the positive penalty parameter which can be adjusted to promote the rate of convergence. Minimizing $L_\rho(\mathbf{f}, \mathbf{z}, \mathbf{u})$ with respect to \mathbf{f} and then with respect to \mathbf{z} , and conducting a multiplier update, yields three steps,

$$\mathbf{f}^{(k+1)} = \underset{\mathbf{f}}{\text{argmin}} \left(\frac{1}{2} \|\mathbf{x} - \mathbf{H}\mathbf{f}\|_2^2 + \rho (\mathbf{u}^{(k)})^T \mathbf{f} + \frac{\rho}{2} \|\mathbf{f} - \mathbf{z}^{(k)}\|_2^2 \right), \quad (10)$$

$$\mathbf{z}^{(k+1)} = \underset{\mathbf{z}}{\text{argmin}} \left(\lambda \|\mathbf{z}\|_p^p + \frac{\rho}{2} \|\mathbf{f}^{(k+1)} - \mathbf{z} + \mathbf{u}^{(k)}\|_2^2 \right), \quad (11)$$

$$\mathbf{u}^{(k+1)} = \mathbf{u}^{(k)} + \mathbf{f}^{(k+1)} - \mathbf{z}^{(k+1)}, \quad (12)$$

where \mathbf{f} -update and \mathbf{z} -update can be accomplished by computing the proximal operator of the convex quadratic term in Eq. (10) and the ℓ_p -norm ($0 \leq p \leq 1$) in Eq. (11), respectively, which will be studied in the following section. Then the \mathbf{u} -update shall be carried out through Eq.

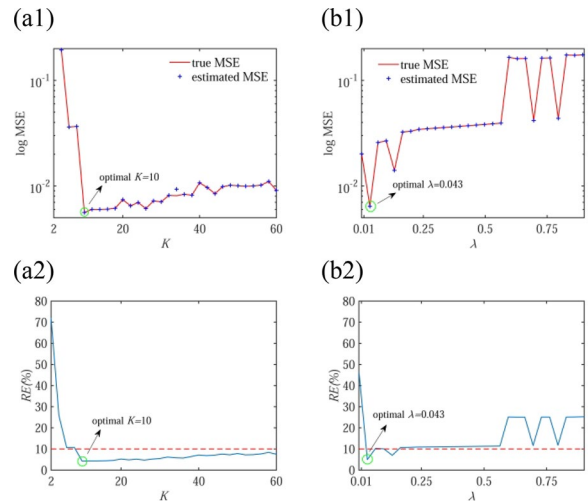


Figure 3 Optimal parameter choosing by minimizing MC-GSURE MSE: **(a1)** Minimizing MC-GSURE MSE by changing K , **(b1)** Minimizing MC-GSURE MSE by changing λ , **(a2)** Results of IFI $\ell_{1/2}$ regularization indicated by REs using different K s, **(b2)** Results of IFI using $\ell_{1/2}$ regularization indicated by REs using different λ s

(12). A critical point of the augmented Lagrangian can be reached in the end [39].

3.2 Resolving Subproblems Using Proximal Operators

The subproblems in Eq. (10) and Eq. (11) can be handled efficiently by proximal operators. Commonly, given a function $h(\mathbf{v})$, its proximal operator is given by [40]:

$$\text{prox}_{h_{\mathbf{v}}}(\mathbf{w}) = \underset{\mathbf{v}}{\text{argmin}} \left\{ h(\mathbf{v}) + \frac{1}{2} \|\mathbf{v} - \mathbf{w}\|_2^2 \right\}, \quad (13)$$

where \mathbf{w} denotes the input vector. To begin with, for \mathbf{f} -update, the proximal operator of the convex quadratic function $h(\mathbf{f}) = \frac{1}{2\rho} \|\mathbf{x} - \mathbf{H}\mathbf{f}\|_2^2 + (\mathbf{u}^{(k)})^T \mathbf{f}$ is taken as,

$$\text{prox}_{h_{\mathbf{f}}}(\mathbf{z}^{(k)}) = \underset{\mathbf{f}}{\text{argmin}} \left\{ h(\mathbf{f}) + \frac{1}{2} \|\mathbf{f} - \mathbf{z}^{(k)}\|_2^2 \right\}, \quad (14)$$

which is equivalent to the minimization in Eq. (10). The optimal solution of Eq. (14) is calculated by taking the derivative with respect to \mathbf{f} and setting it equal to $\mathbf{0}$, that is,

$$(\mathbf{H}^T \mathbf{H} + \rho \mathbf{I}) \mathbf{f}^{(k+1)} - \mathbf{H}^T \mathbf{x} - \rho (\mathbf{z}^{(k)} - \mathbf{u}^{(k)}) = \mathbf{0}, \quad (15)$$

and hence the \mathbf{f} -update can be gained in a closed-form as

$$\mathbf{f}^{(k+1)} = (\mathbf{H}^T \mathbf{H} + \rho \mathbf{I})^{-1} (\mathbf{H}^T \mathbf{x} + \rho (\mathbf{z}^{(k)} - \mathbf{u}^{(k)})). \quad (16)$$

In the end, a compact expression of \mathbf{f} -update step leads to,

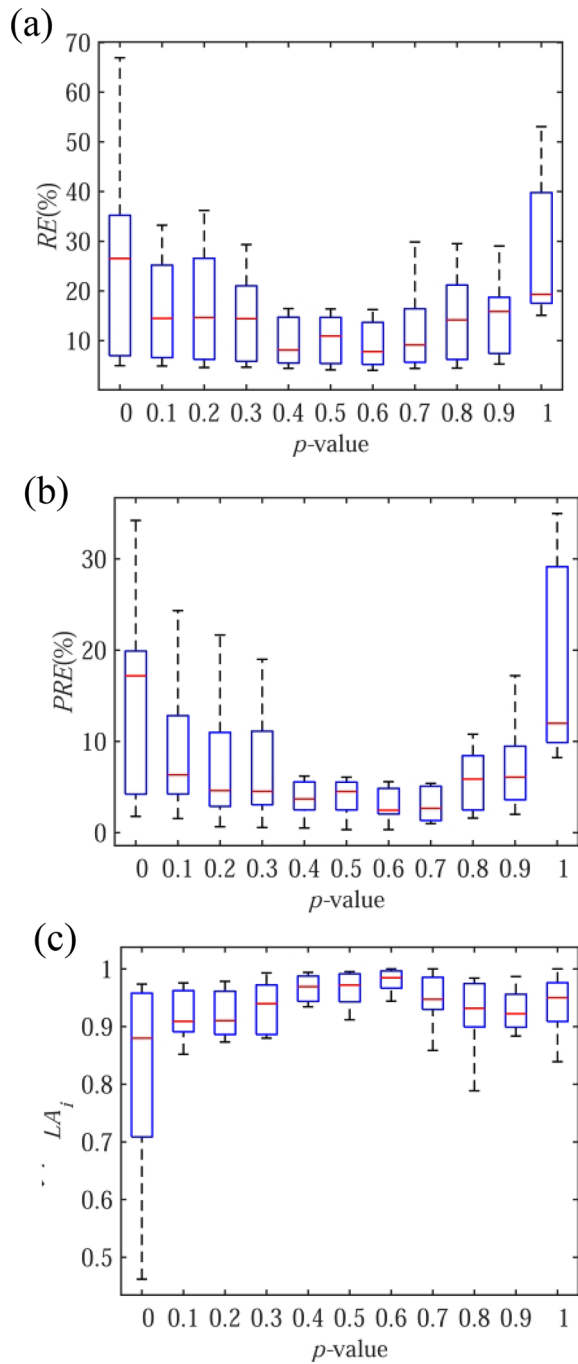


Figure 4 Identification results of nine monitored locations under varying p values: (a) REs, (b) PREs, (c) LA_i s

$$\mathbf{f}^{(k+1)} = \text{prox}_{h_t}(\mathbf{z}^{(k)}). \tag{17}$$

The \mathbf{z} -update can be accomplished by computing the proximal operator of ℓ_p -norm ($0 \leq p \leq 1$). To make the description easy to follow, a general proximal operator form is studied with $h(\mathbf{v}) = \|\mathbf{v}\|_p^p$ scaled by μ , which is,

$$\text{prox}_{h,\mu}(\mathbf{w}) = \underset{\mathbf{v}}{\text{argmin}} \{ \mu \|\mathbf{v}\|_p^p + \frac{1}{2} \|\mathbf{v} - \mathbf{w}\|_2^2 \}. \tag{18}$$

Different p s make for different solutions of Eq. (18), and detailed studies come as follows.

I) When $p = 0$, the corresponding proximal operator known as hard-thresholding [38] is defined component-wise as:

$$\text{prox}_{h,\mu}(\mathbf{w})_i = \begin{cases} 0, & |w_i| \leq T(\mu), \\ w_i, & |w_i| > T(\mu), \end{cases} \tag{19}$$

where w_i represents the i th element in vector \mathbf{w} , and $T(\mu)$ is the threshold, where $T(\mu) = \sqrt{2\mu}$.

II) When $p = 1$, the proximal operator is the familiar soft-thresholding operator [41],

$$\text{prox}_{h,\mu}(\mathbf{w})_i = \begin{cases} 0, & |w_i| \leq T(\mu), \\ \text{sign}(w_i)(|w_i| - \mu), & |w_i| > T(\mu), \end{cases} \tag{20}$$

where $T(\mu) = \mu$.

III) When $0 < p < 1$, the corresponding proximal operator has no analytic solution, but can be resolved via an inexact proximal operator called generalized shrinkage / thresholding (GST) operator [28],

$$\text{prox}_{h,\mu}(\mathbf{w})_i = \begin{cases} 0, & |w_i| \leq T_p(\mu), \\ \text{sign}(w_i)v_i^{(M+1)}, & |w_i| > T_p(\mu), \end{cases} \tag{21}$$

where $T_p(\mu) = (2\mu(1-p))^{\frac{1}{2-p}} + \mu p (2\mu(1-p))^{\frac{p-1}{2-p}}$ is the thresholding value derived in Ref. [28], and $v_i^{(M+1)}$ is the output of $v_i^{(m+1)} = |w_i| - \mu p (v_i^{(m)})^{p-1}$, $m = 0, 1, 2, \dots, M$. Empirically M is chosen as 2, and $v_i^{(0)}$ is initialized as $|w_i|$. Notably, the hard-thresholding and soft-thresholding functions are special cases of GST with $p = 0$ and $p = 1$ [28], and when $p = 1/2$ or $2/3$, a closed-form solution can be deduced [35, 42]. Hence, considering the generalized p values, the GST thresholding is utilized for ℓ_p regularization herein. Accordingly, combining Eq. (11) with Eq. (18), and after some variable substitution, especially $\mathbf{v} = \mathbf{z}$, $\mathbf{w} = \mathbf{f}^{(k+1)} + \mathbf{u}^{(k)}$ and $\mu = \lambda / \rho$, the proximal operator for the \mathbf{z} -update is given by,

$$\text{prox}_{h_{z,\frac{\lambda}{\rho}}}(\mathbf{f}^{(k+1)} + \mathbf{u}^{(k)}) = \underset{\mathbf{z}}{\text{argmin}} \left\{ \frac{\lambda}{\rho} \|\mathbf{z}\|_p^p + \frac{1}{2} \|\mathbf{z} - \mathbf{f}^{(k+1)} - \mathbf{u}^{(k)}\|_2^2 \right\}, \tag{22}$$

and then the update step for \mathbf{z} can be compactly written as,

$$\mathbf{z}^{(k+1)} = \text{prox}_{h_{z,\frac{\lambda}{\rho}}}(\mathbf{f}^{(k+1)} + \mathbf{u}^{(k)}). \tag{23}$$

By virtue of the ADMM, the optimization for problem (8) can be handled succinctly by three main steps, briefly indicated in Eq. (17), Eq. (23) and Eq. (12).

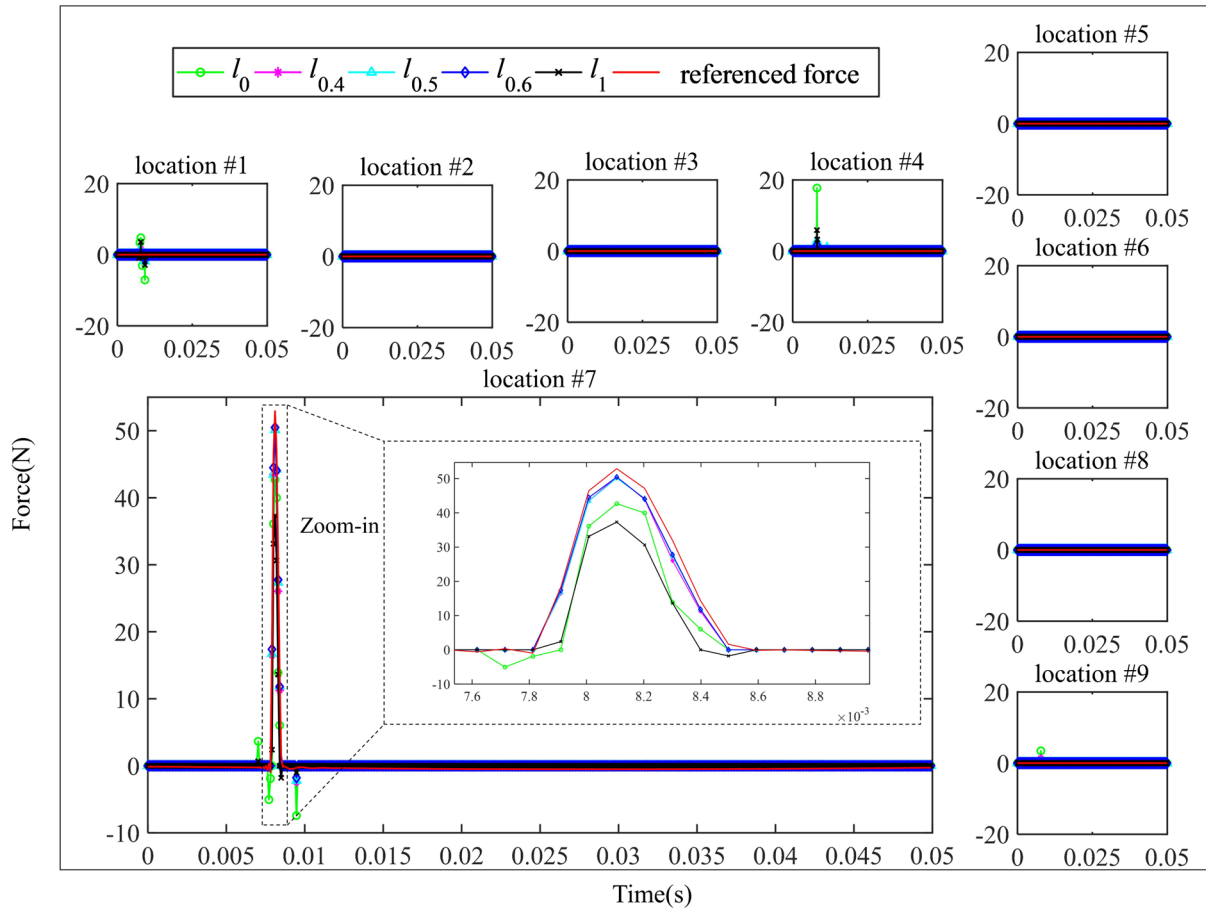


Figure 5 The estimated forces via ℓ_p regularization ($p = 0, 0.4, 0.5, 0.6, 1$) with the true impact force applied at location #7

3.3 Deriving the Adaptive Regularization Parameter Using K -sparsity

As we all know, the results of regularization techniques are quite sensitive and vulnerable to the selection of the regularization parameter λ . And it is generally difficult to choose the optimal λ which mainly depends on the noise level and the transfer matrix [43]. Once noise levels or transfer matrices change, careful and energy-draining operations to find optimal λ are inevitable. To overcome these obstacles, a robust and adaptive strategy for the λ selection is developed according to K -sparsity [35], because IFI is actually a K -sparsity problem in time domain, thanks to its joint space-time sparsity priori. Specifically speaking, the \mathbf{z} -update in Eq. (23) is involved, and \mathbf{z} expects the identical sparsity as \mathbf{f} according to the constraints in Eq. (8). Instead of a fixed λ , the λ can be set adaptively in light of the K -sparsity priori, that is, the adaptive threshold T is set to the K th largest element in the input vector $\mathbf{w}^{(k)} = \mathbf{f}^{(k+1)} + \mathbf{u}^{(k)}$ (in absolute value) at each iteration [35], which is expressed as

$$T^{(k)}(p, \frac{\lambda}{\rho}) = \left| \mathbf{w}^{(k)} \right|_{[K]}, \tag{24}$$

where $\left| \mathbf{w}^{(k)} \right|_{[K]}$ denotes the K th largest component (in absolute value) in the vector $\mathbf{w}^{(k)}$ at the k th iteration. Resolving Eq. (24) can lead to a reliable choice of λ at each iteration, and here an analytic solution of λ can be gained as,

$$\lambda^{(k)} = \frac{\left(\left| \mathbf{w}^{(k)} \right|_{[K]} \right)^{(2-p)}}{p^{(2-p)}(2-2p)^{(p-1)} - 2p + 2}. \tag{25}$$

Finally, the derived ℓ_p regularization algorithm with adaptive regularization parameters named ADMM-SpaRe for IFI is stated in Algorithm 1 (shown in Table 1). Besides, the Algorithm 1 stops when the relative maximum change of adjacent iterations becomes less than a small value ε , say $\varepsilon=10^{-5}$ here, i.e., $\|\mathbf{f}^{(k+1)} - \mathbf{f}^{(k)}\|_{\infty} < \varepsilon \cdot \|\mathbf{f}^{(k)}\|_{\infty}$. Note that early termination in the \mathbf{f} -update and \mathbf{z} -update steps can even give

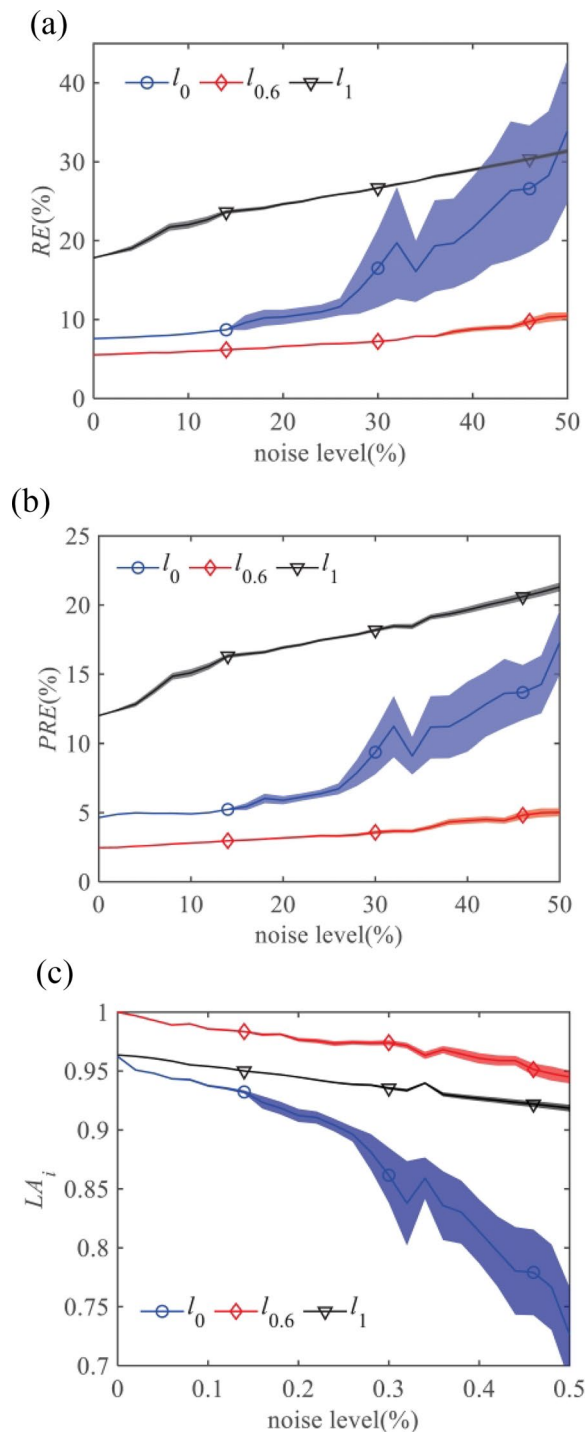


Figure 6 Robustness behaviors of ADMM-SpaRe- l_p ($p = 0, 0.6, 1$) with respect to different noise levels: (a) REs, (b) PREs, (c) LA_i s (The shadow area around each curve denotes ± 3 standard deviation range of 100 trials)

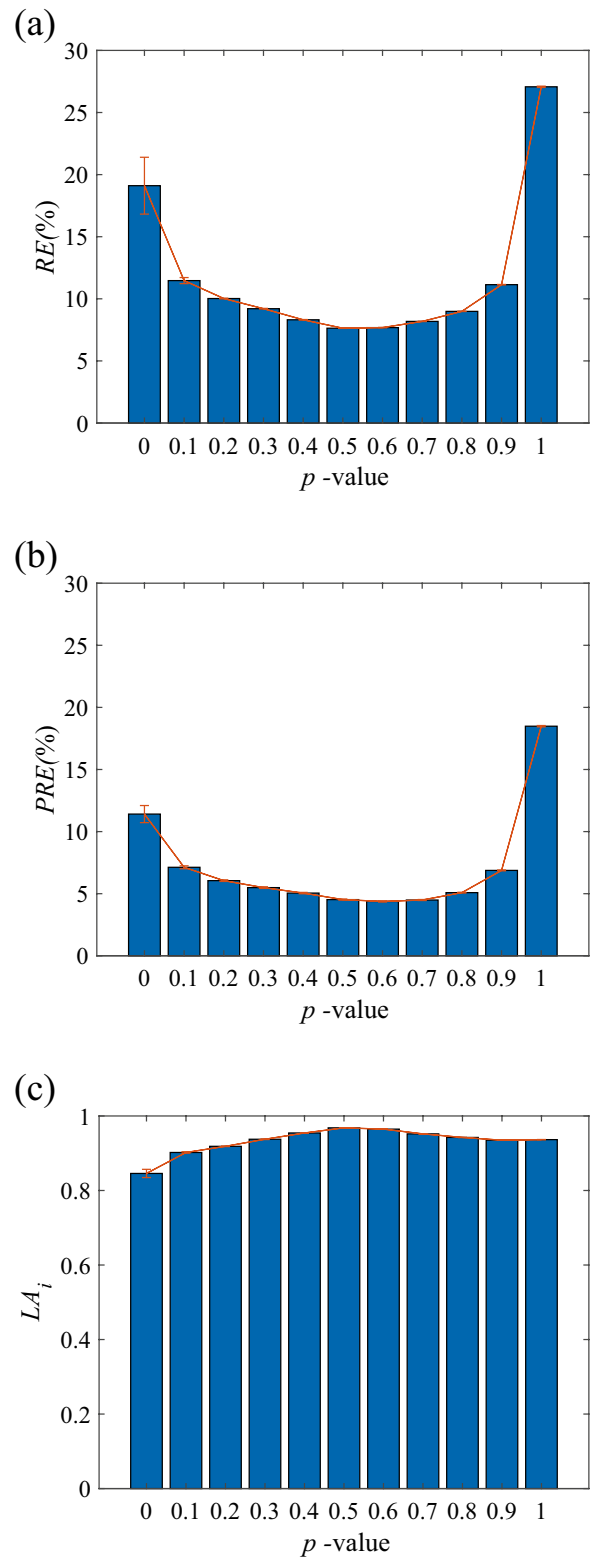


Figure 7 Robustness behaviors of ADMM-SpaRe- l_p ($0 \leq p \leq 1$) under 50% noise level: (a) REs, (b) PREs, (c) LA_i s

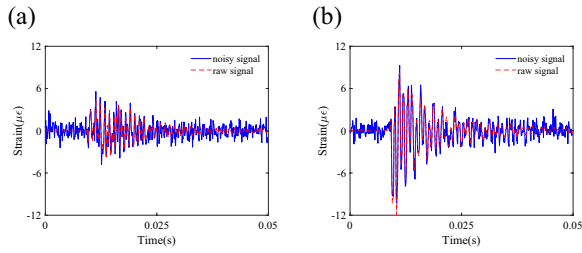


Figure 8 Strain responses with 50% noise level of (a) strain gage #1 and (b) strain gage #9

an overall enhancement in algorithm efficiency [34, 39, 44]. Presetting K makes an adaptive threshold instead of a fixed one. Note that in applications the parameter K can be decided exactly based on the physical prior, or can be set as an upper-bound estimate of the sparsity under discussion via simulation/experimentation studies [35]. In this contribution, K is selected by minimizing MC-GSURE MSE.

3.4 Parameter Setting

There are three parameters including $0 \leq p \leq 1$, $\rho > 0$, $K > 0$ to be determined in Algorithm 1. Firstly, taking sparsity as a prior can bring strong constraints and then reduce the degrees of freedom of the IFI model, which makes it feasible to tackle the under-determined case. Generally speaking, setting $0 \leq p \leq 1$ makes sparse solutions accessible for IFI, but ℓ_1 regularization often produces biased estimates. Numerous studies point out that when $p < 1$, the non-convex ℓ_p regularization can promote sparser and more accurate results than the convex ℓ_1 regularization, but the optimal p is usually different in different applications [28]. For example, $\ell_{2/3}$ performs better than $\ell_{1/2}$ in image deconvolution [42]. Therefore, the optimal p is studied by investigating different p s in a fine division between 0 and 1 in the following experiments.

Secondly, for the sake of improving convergence, the penalty parameter ρ is adjusted using residual balancing strategy [45], i.e.,

$$\rho^{(k+1)} = \begin{cases} 2\rho^{(k)}, & \left\| \mathbf{r}_{\text{primal}}^{(k)} \right\|_2 > 10 \left\| \mathbf{r}_{\text{dual}}^{(k)} \right\|_2, \\ 0.5\rho^{(k)}, & \left\| \mathbf{r}_{\text{dual}}^{(k)} \right\|_2 > 10 \left\| \mathbf{r}_{\text{primal}}^{(k)} \right\|_2, \\ \rho^{(k)}, & \text{otherwise,} \end{cases} \quad (26)$$

where $\mathbf{r}^{(k)} = \tilde{\mathbf{f}}^{(k)} - \mathbf{z}^{(k)}$ and $\mathbf{s}^{(k)} = -\rho(\mathbf{z}^{(k+1)} - \mathbf{z}^{(k)})$ are the primal and dual residuals in the k th iteration of ADMM-SpaRe, respectively.

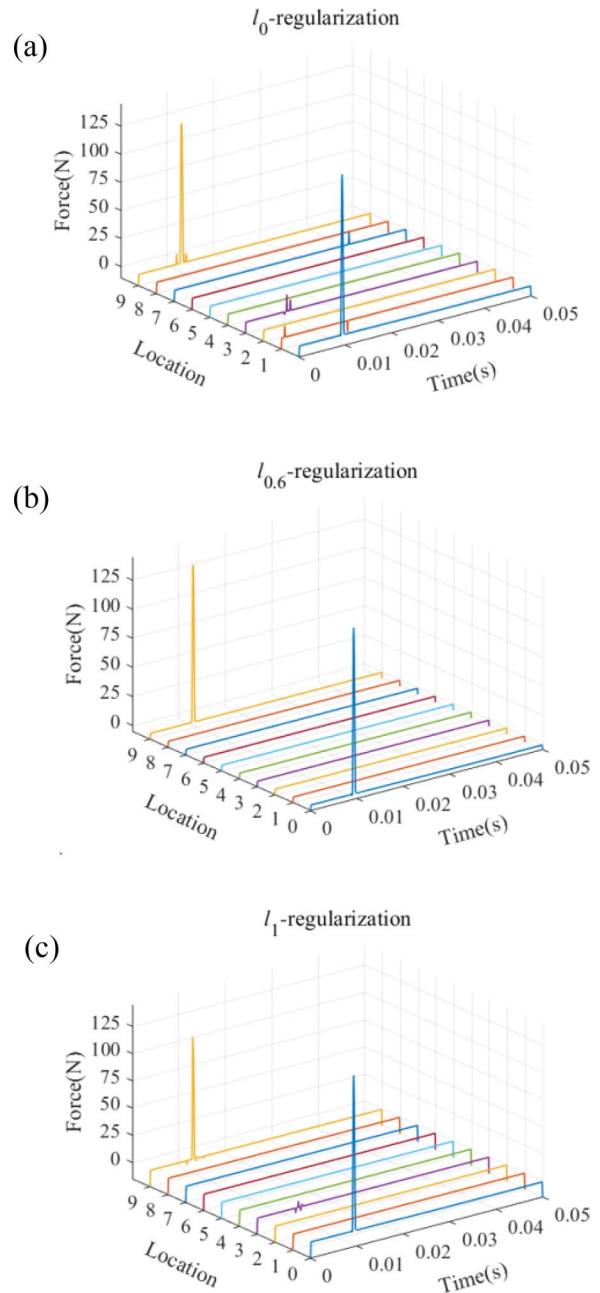


Figure 9 IFI results of ADMM-SpaRe- ℓ_p ($p = 0, 0.6, 1$) under 50% noise level: (a) ℓ_0 regularization, (b) $\ell_{0.6}$ regularization, (c) ℓ_1 regularization (The exact impact force is illustrated at location #0)

For a better choice of K in practice, a practical and reliable thought is based on minimizing MSE. However, the identification MSE can not be known in practice. MC-GSURE is used to estimate MSE availablely. Due to a rank-deficient model dealt with in the under-determined IFI case, generalized SURE to get an unbiased estimate of MSE is defined as [36],

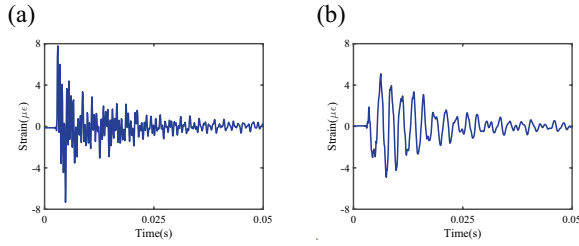


Figure 10 Strain responses in the single-impact case from (a) strain gage #1 and (b) strain gage #9

$$E\left(\|\mathbf{P}(h_K(\mathbf{u}) - \mathbf{f})\|^2\right) = \|\mathbf{P}\mathbf{f}\|^2 + \|\mathbf{P}h_K(\mathbf{u})\|^2 + 2\text{div}_{\mathbf{u}}(\mathbf{P}h_K(\mathbf{u})) - 2h_K^T(\mathbf{u})\hat{\mathbf{f}}_{\text{ML}}, \quad (27)$$

where \mathbf{P} is a projection matrix $\mathbf{P} := \mathbf{H}^T(\mathbf{H}\mathbf{H}^T)^{-1}\mathbf{H}$, $h_K(\mathbf{u})$ returns the identification results of Eq. (6) using K -sparsity, $\mathbf{u} = \frac{1}{\sigma^2}\mathbf{H}^T\mathbf{x}$ (σ is the standard deviation of noise) represents the sufficient statistic for the model, $\hat{\mathbf{f}}_{\text{ML}} = \mathbf{H}^T(\mathbf{H}\mathbf{H}^T)^{-1}\mathbf{x}$ is the maximum likelihood estimation, and the divergence $\text{div}_{\mathbf{u}}(\mathbf{P}h_K(\mathbf{u}))$ is approximated by the MC method as [46]:

$$\text{div}_{\mathbf{u}}(\mathbf{P}h_K(\mathbf{u})) \approx \mathbf{b}^T \mathbf{P} \frac{h_K(\mathbf{u} + \delta\mathbf{b}) - h_K(\mathbf{u})}{\delta}, \quad (28)$$

where \mathbf{b} is a Gaussian vector with zero mean and unit standard deviation, and δ is a small positive parameter. Thus far, an overall flowchart of the proposed ADMM-SpaRe algorithm for IFI is given in Figure 1.

4 Experimental Validation

In this section, a series of laboratory experiments are implemented on a composite panel to verify the effectiveness and investigate the performance of the proposed ADMM-SpaRe method for IFI tasks. Impact forces are identified utilizing only structural responses, and impact events can be localized and reconstructed concurrently based on an under-determined sensor configuration. The optimal sparsity value K is investigated by calculating MC-GSURE MSE. A representative p is chosen for IFI through experimental study. The robustness of ADMM-SpaRe to noise interference is also examined.

4.1 Experimental Setup

An aircraft skin-like composite laminated plate, which is fabricated by T700/QY8911 carbon fiber reinforced pre-impregnated unidirectional layers and clamped at both ends, is limned in Figure 2, with the size of $400 \times 300 \times 6$ mm and the lay-up: $[\pm 45/0/-45/90]_{6s}$.

Firstly, as shown in Figure 2(a), impact forces are produced by an instrumented hammer with a force transducer (PCB 086C03, sensitivity 2.25 mV/N), and the vibration data (i.e., strain responses) are measured by ten strain gages (PCB 740B02). Only two strain gages (strain gage 1 and strain gage 9, with sensitivity 52.2 mV/g and 48.6 mV/g, separately) are utilized here for IFI. Figure 2(b) visualizes the spatial arrangement of the key points on the laminate: nine uniformly distributed points are monitored as potential impact locations; ten strain gages are equally mounted on both sides of the monitoring area. All of these points fall on the grid with size of 50×50 mm.

Secondly, the data including impact forces and strain responses are recorded by LMS Test.Lab system synchronously with a sampling frequency of 10240 Hz. Thirdly, the transfer matrix \mathbf{H} is constructed experimentally, which is briefly divided into two steps: (i) The IRF $h_{ij}(t)$ between the output location i and input location j can be gained by means of inverse fast Fourier transform (IFFT) of the frequency response function (FRF) $h_{ij}(w)$ which can be acquired by impact testing via the LMS modal testing module; (ii) The block Toeplitz-like matrix \mathbf{H} in Eq. (5) is assembled according to Eq. (4). The analyzed data length N of each discrete IRF is 512, making each submatrix in Eq. (4) have a dimension of 512. Herein, only two strain gages are employed to monitor the nine potential impact positions, resulting in a quite under-determined system with the transfer matrix $\mathbf{H} \in \mathbb{R}^{1024 \times 4608}$. Finally, all experimental analyses are conducted under MATLAB 2018b and on a personal computer equipped with Intel^(R) Core^(TM) i5-8400, 24 GB RAM.

To evaluate the performance of ADMM-SpaRe quantitatively, several accuracy assessment indicators are defined. Note that the impact force measured by the force transducer attached on the hammer is taken as reference in the experiments. Firstly, the global relative error (RE) between the identified force vector $\tilde{\mathbf{f}}$ and the referenced one \mathbf{f} is calculated as:

$$RE(\%) = \frac{\|\tilde{\mathbf{f}} - \mathbf{f}\|_2}{\|\mathbf{f}\|_2} \times 100\%, \quad (29)$$

and then, the RE at each location i can be computed as:

$$RE_i(\%) = \frac{\|\tilde{\mathbf{f}}_i - \mathbf{f}_i\|_2}{\|\mathbf{f}_i\|_2} \times 100\%. \quad (30)$$

Next, the peak relative error (PRE) at the impact location i , assessing the reconstruction quality of the impact amplitude which matters much for IFI, is expressed as:

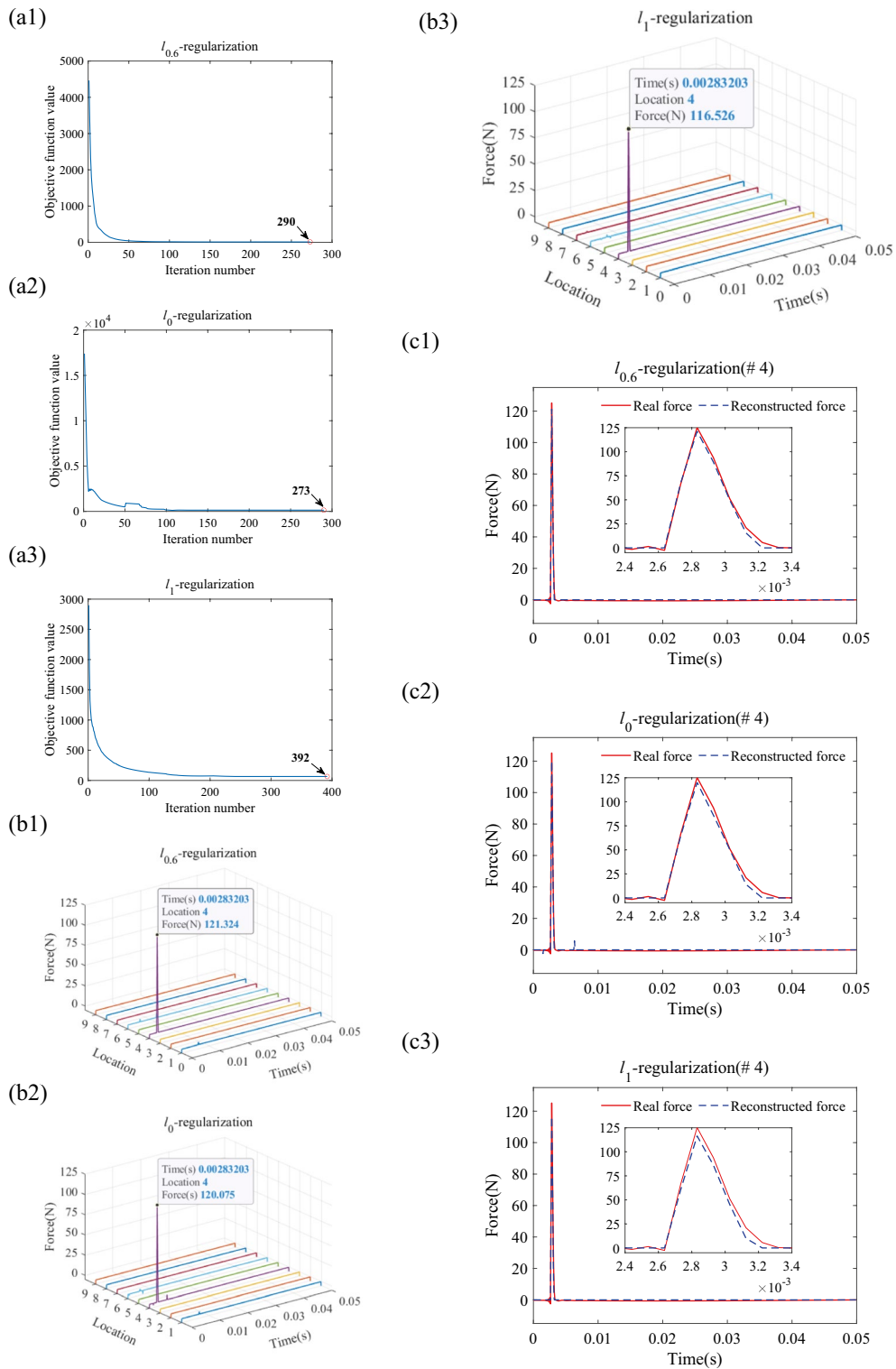


Figure 11 Experimental results of IFI in the single-impact case: (a1–a3) The objective function values during the iteration using $l_{0.6}$ regularization, l_0 regularization and l_1 regularization, (b1–b3) Localization results of $l_{0.6}$ regularization, l_0 regularization and l_1 regularization, (c1–c3) Time history on the impact point #4 via $l_{0.6}$ regularization, l_0 regularization and l_1 regularization

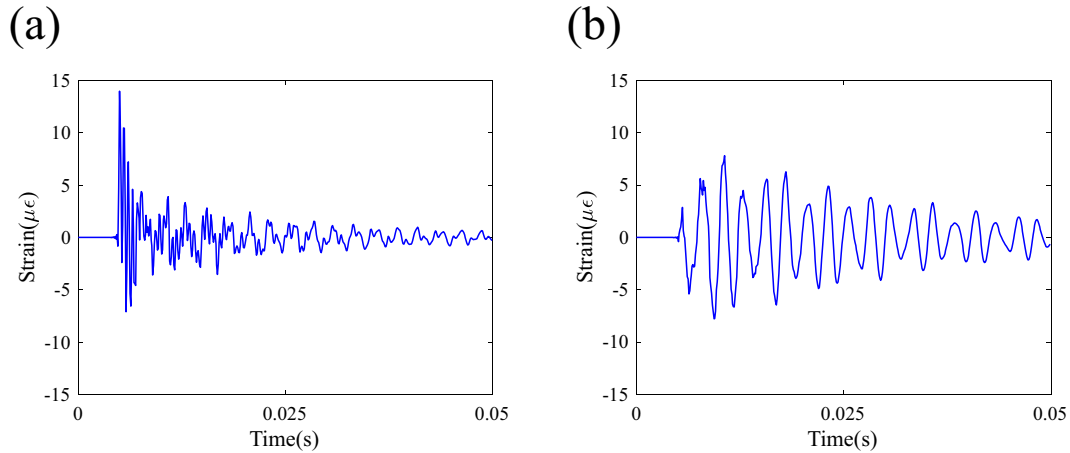


Figure 12 Strain responses in the double-impact case from (a) strain gage #1 and (b) strain gage #9

$$PRE_i(\%) = \frac{\|\tilde{f}_{p_i} - f_{p_i}\|_2}{\|\tilde{f}_{p_i}\|_2} \times 100\%. \quad (31)$$

Finally, an indicator LA_i at the impact location i , evaluating the localization accuracy (LA), is represented as:

$$LA_i = \frac{\|\tilde{\mathbf{f}}_i\|_2}{\sum_{i=1}^{n_f} \|\tilde{\mathbf{f}}_i\|_2}. \quad (32)$$

In this work, it is assumed that one impact force is exerted on one of the potential impact locations during the observation period. Theoretically, LA_i should be one for the actual impact position, and be zero for non-impact locations.

4.2 Sparsity Estimation via MC-GSURE

As aforementioned, once K is set, adaptive regularization parameters are updated automatically at each iteration according to Eq. (25). K is actually determined by the sparse physical priori of the impact forces, and requires no adjustment regardless of changes in the noise level of the measurement. Next, how to choose the optimal K and why K -sparsity is used instead of a fixed λ are respectively stated through experimental studies. Without loss of generality, p is equal to $1/2$ and the true impact force acts on #1. 31 different values are allocated to K and λ in a range of $0.01 - 1$ (in increments of 0.033) and $2 - 60$ (in increments of 2) respectively. For MC-GSURE MSE computing, the noise level of the measurement can be obtained by the well-known mean absolute derivative (MAD) rule [47]. For the MC process in Eq. (28), δ is set to 10^{-5} and an average of five independent realizations

are taken. Then the optimal λ and K are both found by minimizing MSE, as shown in Figure 3.

From Figure 3(a1) and (a2), firstly, pretty accurate estimates of MSE can be acquired by MC-GSURE. Secondly, for K -sparsity, the optimal $K = 10$ is obtained, exactly matching with the sparsity of the true impact force. From Figure 3(b1), when K is larger than the real sparsity, a wide range of overestimations of K can lead to stable and high-accuracy solutions, and when $K = 60$, six times the real K , the accurate identification accuracy can be realized with RE less than 10%. Looking into Figure 3(b2), the fixed strategy is not comparable to the K -sparsity strategy with lower accuracy. According to the current division of λ , there is a small adjustment range and consequent results are unstable. What is noteworthy is that once K is set, regularization parameters are updated automatically without considering noise levels. However, when the fixed λ strategy is used, the optimal λ needs to be adjusted continually according to the corresponding noise level [43]. As a result, the K -sparsity strategy based on MC-GSURE is employed in the following experimental study.

4.3 The Optimal Selection for p

Regrading ℓ_p regularization, the optimal p varies in different application areas [28, 48]. Thus, the optimal p for IFI is investigated. The impact forces applied at nine different locations in Figure 2(b) are individually identified by ADMM-SpaRe with p ranging from 0 to 1 at the interval of 0.1. Then, the box-plots in Figure 4 give the identified results indicated by REs , $PREs$, and LA_i s, and each box visually shows the identification accuracy of all nine monitored positions under each p value. The box-plots say that ADMM-SpaRe possesses good identification

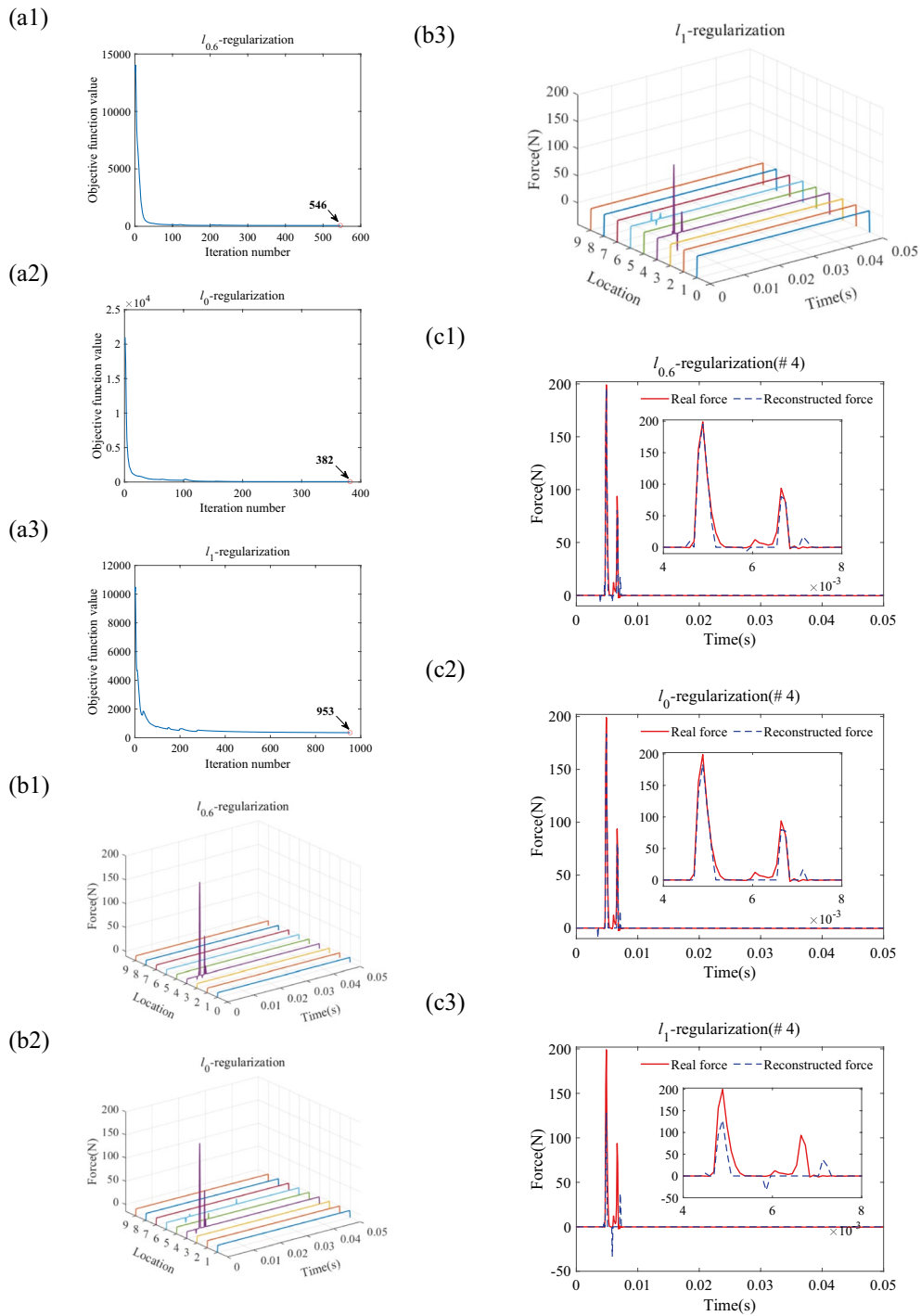


Figure 13 Experimental results of IFI in the double-impact case: **(a1–a3)** The objective function values during the iteration using $l_{0.6}$ regularization, l_0 regularization and l_1 regularization, **(b1–b3)** Localization results of $l_{0.6}$ regularization, l_0 regularization and l_1 regularization, **(c1–c3)** Time history on the impact point #4 via $l_{0.6}$ regularization, l_0 regularization and l_1 regularization

accuracy and stability when $p = 0.4 - 0.6$. To be specific, when setting $p = 0.4, 0.5$ and 0.6 , induced REs and $PREs$ are less than 20% and 10% respectively, and $LA_i s$ are

more than 0.9, which are hard to be guaranteed by other p settings, especially when $p = 0$ or 1.

Moreover, when $p = 0.6$, ADMM-SpaRe achieves the highest identification accuracy. An exemplary

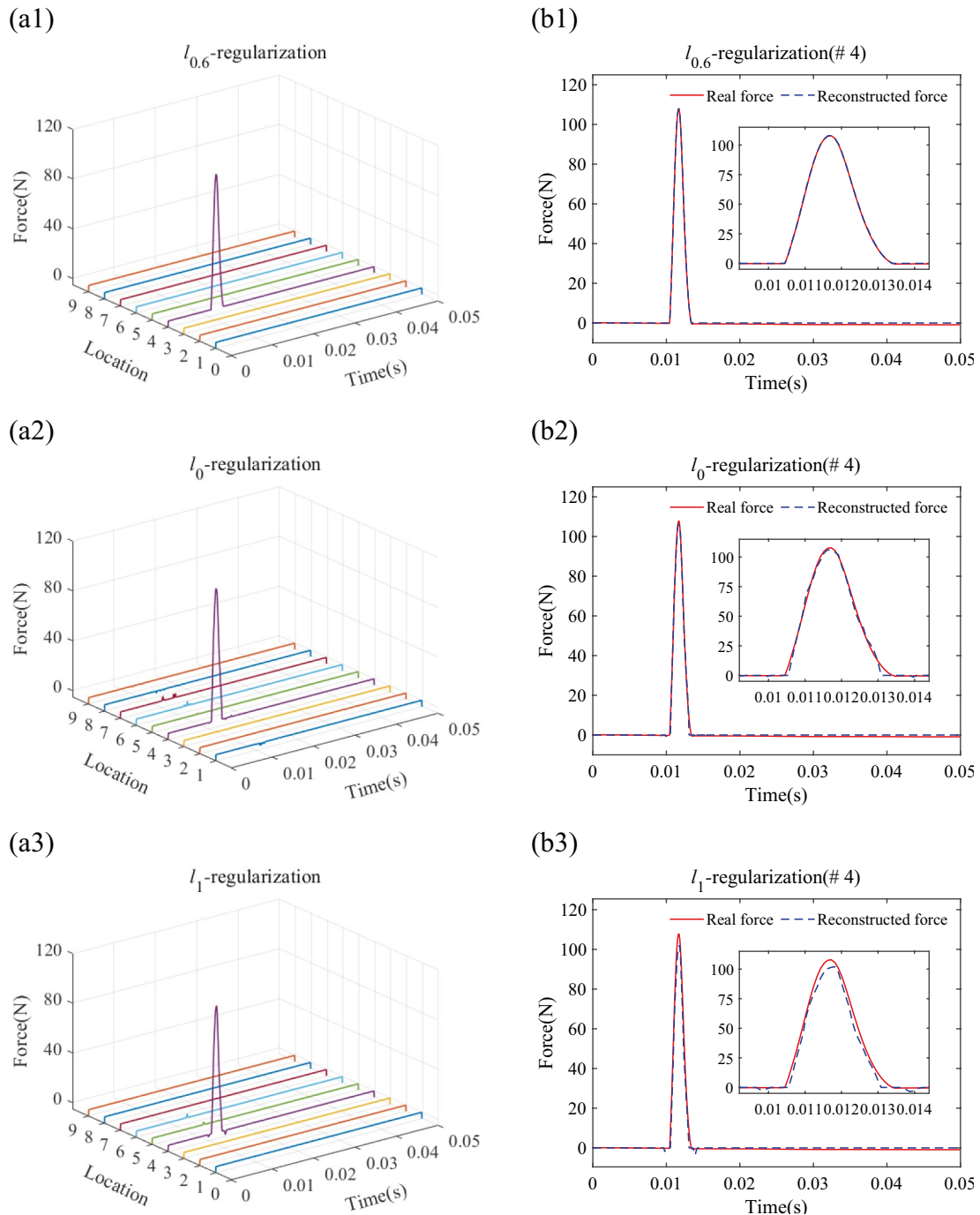


Figure 14 IFI experimental results of rubber hammer cap impact: (a1–a3) Localization results of $l_{0.6}$ regularization, l_0 regularization and l_1 regularization, (b1–b3) Time history on the impact point #4 via $l_{0.6}$ regularization, l_0 regularization and l_1 regularization

description can be found in Figure 5, where the impact force is applied on #7 and the results are estimated by l_p ($p = 0, 0.4, 0.5, 0.6, 1$) regularization. It shows that the false forces identified by l_0 and l_1 regularization occur on the non-impact positions #1, #4 and #9, and along

comes the poor reconstruction accuracy on the exact impact position #7 with $REi_{l_0} = 36.5\%$, $REi_{l_1} = 42.4\%$, $PREi_{l_0} = 19.4\%$, and $PREi_{l_1} = 29.5\%$. But the estimations from $l_{0.4}$, $l_{0.5}$ and $l_{0.6}$ regularization can avoid these problems, and the indicators with respect to

Table 1 ADMM-SpaRe algorithm pseudo code

Algorithm 1 ADMM-SpaRe for IFI	
Require:	$0 \leq p \leq 1, \rho > 0, K > 0.$
Initialize:	$k = 0, \mathbf{f}^{(0)} = \mathbf{0}, \mathbf{z}^{(0)} = \mathbf{0}, \mathbf{u}^{(0)} = \mathbf{0}.$
Output:	$\mathbf{f}^{(k+1)}.$
1.	$\mathbf{f}^{(k+1)} = \text{prox}_{h_f}(\mathbf{z}^{(k)}),$
2.	$\lambda^{(k)} = \frac{\left(\ \mathbf{f}^{(k+1)} + \mathbf{u}^{(k)}\ _{K1}\right)^{(2-p)}}{p^{(2-p)}(2-2p)^{(p-1)} - 2p + 2},$
3.	$\mathbf{z}^{(k+1)} = \text{prox}_{h_z, \frac{\lambda^{(k)}}{\rho}}(\mathbf{f}^{(k+1)} + \mathbf{u}^{(k)}),$
4.	$\mathbf{u}^{(k+1)} = \mathbf{u}^{(k)} + \mathbf{f}^{(k+1)} - \mathbf{z}^{(k+1)},$
5.	$k = k + 1,$
6.	Repeat until convergence.

reconstruction accuracy on position #7 are, respectively, $REi_{\ell_{0.4}} = 13.7\%$, $REi_{\ell_{0.5}} = 12.9\%$, $REi_{\ell_{0.6}} = 12.4\%$, $PREi_{\ell_{0.4}} = 4.5\%$, $PREi_{\ell_{0.5}} = 5.3\%$, and $PREi_{\ell_{0.6}} = 4.4\%$, and $\ell_{0.6}$ regularization achieves the highest identification accuracy. Therefore, $p = 0.6$ can be taken as the preferred representative of ℓ_p regularization for IFI because of its high and stable identification accuracy.

4.4 Robustness to Noise Interference

Low noise levels are involved in laboratory experiments indeed. In order to reveal the robustness of ADMM-SpaRe- $\ell_{0.6}$ regularization to noise interference, a noise model is taken into consideration as follows:

$$\tilde{\mathbf{x}} = \mathbf{x} + \beta\sigma \text{randn}(N, 1), \quad (33)$$

where \mathbf{x} and $\tilde{\mathbf{x}} \in \mathbb{R}^N$ denote the original measured signals and signals with additive noise, β is the noise level, respectively, σ signifies the standard deviation of the measured data, and $\text{randn}(N, 1)$ generates values from a normal distribution with zero mean and unit standard deviation. In this study case, the real impact force is exerted on location #9 and the strain responses are still collected by sensors #1 and #9 to ensure generality. Subsequently, β accounts for different noise levels, varying from 0 to 50% in 2% increments. IFI is realized using ADMM-SpaRe- $\ell_{0.6}$, and the outcomes of ℓ_0 and ℓ_1 regularization are also considered for comparison, solved by the well-known hard and soft thresholding formulas, respectively. To eliminate the randomness, 100 independent realizations are performed for different methods under each noise level. Figure 6 shows the average values of indicators including RE, PRE_i , and LA_i .

As described in Figure 6, $\ell_{0.6}$ obtains the best robustness behavior over ℓ_0 and ℓ_1 . In particular, despite the increase of noise, $\ell_{0.6}$ regularization can achieve high performances under 50% noise level, keeping the REs less than 10%, the PREs less than 5%, and the LA_i s more than

0.95. Looking into the results of ℓ_1 regularization, large identification errors appear under each noise level, inferior to $\ell_{0.6}$ regularization. Besides, reasonable identification results can be acquired through ℓ_0 regularization under low noise level, i.e., under less than 15%, as displayed in Figure 6, while identification precision rapidly declines as the noise level rises up.

To better observe the robustness to noise, the indicators representing the identification accuracy of ℓ_p ($0 \leq p \leq 1$) regularization are displayed in Figure 7 under the 50% noise level after 100 independent realizations. It can be discovered that $\ell_{0.6}$ regularization gains the highest identification accuracy, while the accuracy decreases with p s away from 0.6. The noisy signals under the 50% noise level are shown in Figure 8. Correspondingly, detailed IFI results of ℓ_p ($p = 0, 0.6, 1$), covering force time history and impact localization, are illustrated in Figure 9. It can be found visually that spurious forces appear on the non-impact positions, especially in the results produced by ℓ_0 and ℓ_1 regularization, and by contrast, $\ell_{0.6}$ regularization can perform better to alleviate this problem. In short, it is justified that $\ell_{0.6}$ regularization is more powerful than ℓ_0 and ℓ_1 regularization, and ℓ_0 regularization is competitive to ℓ_1 regularization under relatively low noise level.

4.5 IFI Results and Discussion

In this case, for the sake of generality, impact forces generated by the impact hammer with a steel hammer cap are applied to a randomly selected location #4 from nine potential locations as displayed in Figure 2(b). Also, the responses are collected by strain gage #1 and #9, as shown in Figure 10. As previously mentioned, the noise levels are low in experimental scenarios. IFI is accomplished by the proposed ADMM-SpaRe- ℓ_p method with $p = 0.6$, and additionally the results produced by ℓ_0 and ℓ_1 regularization are taken as comparisons.

Figure 11 shows the identification results of the three regularization methods, containing convergence curves, localization and time history reconstruction results. As described in Figure 11(a1), (a2) and (a3), after 273, 290 and 392 iterations, three regularization methods, i.e., $p = 0, 0.6, 1$, solved by ADMM-SpaRe converge to their approximate minimizers, consuming 22.9 s, 24.8 s and 30.6 s respectively. $\ell_{0.6}$ converges faster than the other two methods, and also owns a higher solution accuracy with $RE_{\ell_{0.6}} = 9.7\%$, besides, $RE_{\ell_0} = 11.5\%$ and $RE_{\ell_1} = 12.5\%$ here. Further, from Figure 11(b1), (b2) and (b3), three regularization methods all have relatively high localization accuracy with LA_i s more than 0.9, respectively, $LAi_{\ell_{0.6}} = 0.94$, $LAi_{\ell_0} = 0.93$, $LAi_{\ell_1} = 0.97$. Despite that ℓ_1 regularization can result in high localization accuracy, ℓ_1 regularization likely causes biased estimations, underestimating the amplitude of impact forces.

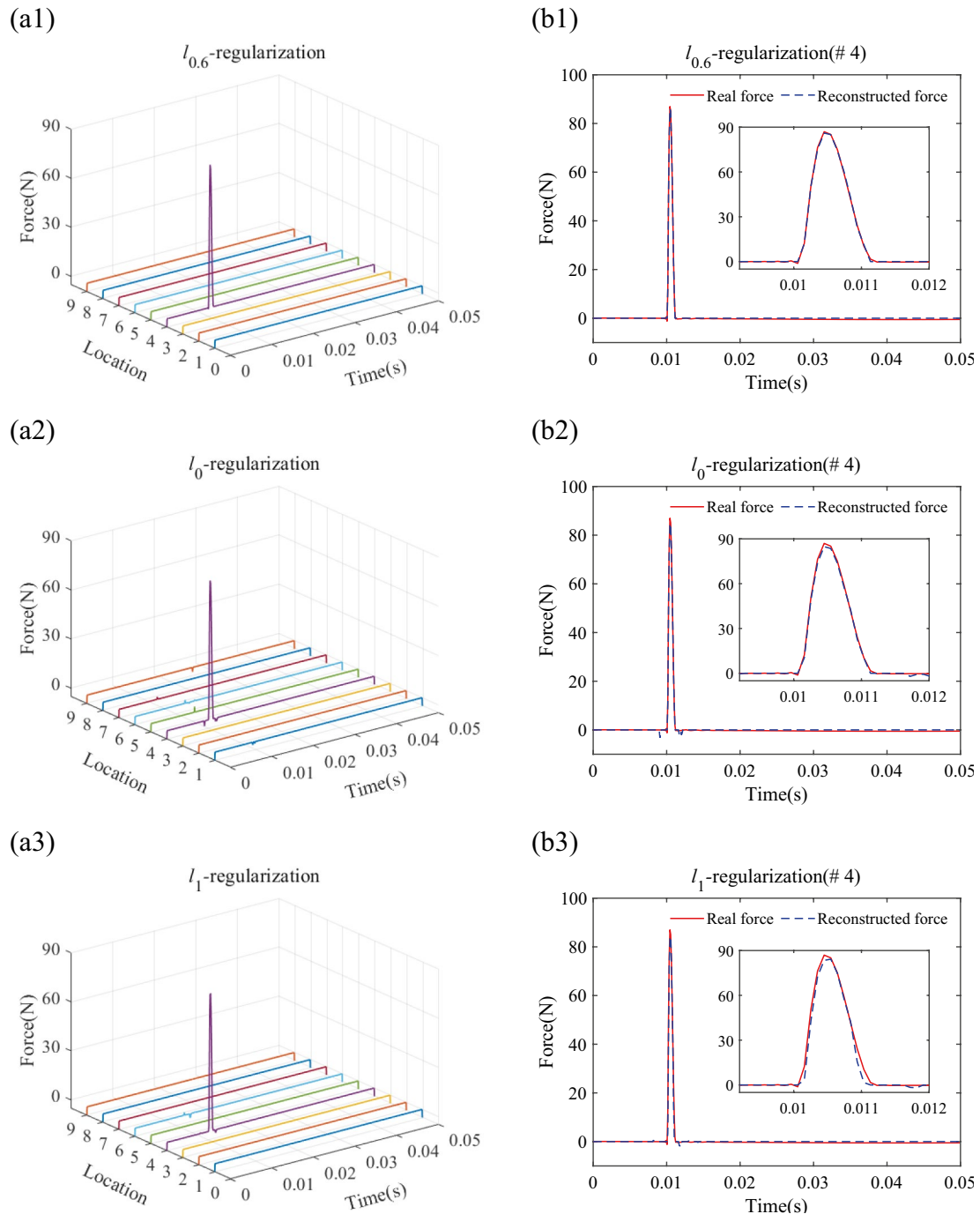


Figure 15 IFI experimental results of plastic hammer cap impact: (a1–a3) Localization results of $\ell_{0.6}$ regularization, ℓ_0 regularization and ℓ_1 regularization, (b1–b3) Time history on the impact point #4 via $\ell_{0.6}$ regularization, ℓ_0 regularization and ℓ_1 regularization

These are not hard to be found from the local analysis of identification results as exhibited in Figure 11(c1), (c2) and (c3), in detail, $PREi_{\ell_{0.6}} = 3.1\%$, $PREi_{\ell_0} = 4.1\%$, $PREi_{\ell_1} = 7.0\%$, and $REi_{\ell_{0.6}} = 3.1\%$, $REi_{\ell_0} = 4.1\%$, $REi_{\ell_1} = 7.0\%$. But the profiles of identified impact forces

from three regularization methods solved by ADMM-SpaRe all match closely with that of the referenced one. On the whole, $\ell_{0.6}$ regularization outperforms the other two regularization methods for IFI tasks .

Table 2 IFI result errors of plastic hammer cap impact case (%)

Error	RE	LAI	REI	PRE
$\ell_{0.6}$	5.5	1.00	5.0	1.0
ℓ_0	6.6	0.98	5.9	2.5
ℓ_1	10.9	0.96	10.7	3.1

In experimental tests, an interesting phenomenon that cannot be ignored is that double-impact sometimes occurs. In this case, the double-impact produced by the impact hammer on #4 is identified using the same three regularization methods. Figure 12 illustrates the strain responses gathered by strain gages #1 and #9 separately, and it is hard to tell whether a double-impact occurs. On this occasion, $\ell_{0.6}$ regularization still retains the highest identification accuracy with $RE_{\ell_{0.6}} = 16.9\%$, compared to $RE_{\ell_0} = 18.7\%$ for ℓ_0 regularization. Notably, ℓ_1 regularization performs unsatisfyingly with $RE_{\ell_1} = 60.1\%$. Then, from Figure 13(b1), $\ell_{0.6}$ regularization is able to fully realize the localization with $LAI_{\ell_{0.6}} = 1$. However, as can be seen from Figure 13(b2) and (b3), ℓ_0 and ℓ_1 regularization fail to do so due to spurious forces appearing at the unloading positions, with $LAI_{\ell_0} = 0.89$ and $LAI_{\ell_1} = 0.87$. Through local analysis of the identified results, it can be discovered that the time history of impact forces can be well-recovered by $\ell_{0.6}$ regularization with $REi_{\ell_{0.6}} = 16.9\%$, and next comes ℓ_0 regularization with $REi_{\ell_0} = 17.1\%$. While ℓ_1 regularization fails with $REi_{\ell_1} = 59.5\%$. Overall, the $\ell_{0.6}$ regularization method solved by ADMMSpaRe is more powerful than the other two methods, and ℓ_0 regularization is comparable to $\ell_{0.6}$ regularization in this case, but ℓ_1 regularization cannot manage to realize the identification under this double-impact circumstance.

In order to further verify the performance of the proposed method in identifying impact forces with different shapes, a rubber hammer cap and a plastic hammer cap are used on the impact hammer to impact the #4 position respectively (Figure 13).

In the case of rubber hammer cap, the impact force localization and time-history reconstruction results of $\ell_{0.6}$, ℓ_0 and ℓ_1 regularization methods are shown in Figure 14. It can be seen from Figure 14(a1–a3) that all three methods can accurately localize the impact force, but the global identification result of $\ell_{0.6}$ regularization is most consistent with the spatial sparsity of the impact force, with $RE_{\ell_{0.6}} = 4.0\%$ and $LAI_{\ell_{0.6}} = 1.00$. The global relative errors and localization accuracy of the other two methods are $RE_{\ell_0} = 6.8\%$, $RE_{\ell_1} = 10.7\%$, and $LAI_{\ell_0} = 0.94$, $LAI_{\ell_1} = 0.98$, respectively. It can be observed from the reconstruction results Figure 14(b1–b3) that the reconstruction accuracy of $\ell_{0.6}$ regularization is the highest,

and the identified impact amplitude is also closest to the real force, with $REi_{\ell_{0.6}} = 4.0\%$ and $PREi_{\ell_{0.6}} = 0.2\%$. In contrast, the time-history reconstruction errors of ℓ_0 and ℓ_1 regularization methods are $REi_{\ell_0} = 6.3\%$, $REi_{\ell_1} = 10.6\%$, $PREi_{\ell_0} = 1.6\%$, and $PREi_{\ell_1} = 5.4\%$.

In the case of plastic hammer cap, the impact force identification results of $\ell_{0.6}$, ℓ_0 and ℓ_1 regularization methods are shown in Figure 15. The same conclusion can be drawn, that is, the impact force localization and reconstruction results of $\ell_{0.6}$ regularization match the real impact situation best. By quantifying the quality of the identification results of the three methods, the identification errors of these three methods can be obtained as listed in Table 2. Therefore, it can be concluded that $\ell_{0.6}$ regularization can reconstruct and localize impact forces of different shapes with higher accuracy.

5 Conclusions

This paper develops an ADMM-based ℓ_p sparse regularization method termed ADMM-SpaRe to cope with the ill-posed IFI inverse problem. Unlike the previous algorithms which approximate the minimum of the nonconvex ℓ_p -minimization by optimizing the proxy functions. ADMM-SpaRe splits the complicated and variable-coupled IFI model into three easier subproblems, and each subproblem can be resolved directly by its proximal operator with high accuracy. Then force reconstruction and impact localization are realized simultaneously with the under-determined sensor configuration where merely two strain gages monitoring nine potential impact locations. To tackle the regularization parameter selection problem, the K -sparsity strategy on account of the joint space-time sparsity priori of IFI is adopted. The optimal K can be accurately found by minimizing the MC-GSURE MSE. A wider range of K s can be chosen to achieve accurate IFI, and once K is set, regularization parameters are updated automatically at each iteration and require no constant fine-tuning, making ADMM-SpaRe an adaptive and robust approach. Moreover, the optimal $p = 0.6$ is recommended for the IFI problem through experimental comparative studies, which can promote sparser and more accurate solutions. Then, to verify the robustness of ADMM-SpaRe to noise, different levels of white Gaussian noise are added into the measured signals. $\ell_{0.6}$ regularization can accomplish relatively accurate IFI even under 50% noise level. Finally, additional impact scenarios including single impact and double impact, rubber hammer cap impact, and plastic hammer cap impact are investigated. It is found that $\ell_{0.6}$ regularization adopting GST thresholding performs better than the ℓ_0 and ℓ_1 regularization conducted using classic

soft thresholding and hard thresholding. In addition, the proposed method is applicable to the impact force identification of different impact times and impact morphologies.

Acknowledgements

Not applicable

Authors' Contributions

YW, JL, BQ and WH were in charge of theoretical derivation; LC, JL are responsible for conducting experiments and data acquisition; YW and LC were assisted with data interpretation and analysis; YW and LC wrote the manuscript; JL, BQ, and XC were responsible for critically revising the manuscript for the intellectual content. All authors read and approved the final manuscript.

Funding

Supported by National Natural Science Foundation of China (Grant Nos. 52305127, 52075414) and China Postdoctoral Science Foundation (Grant No. 2021M702595).

Data availability

The data that support the findings of this study are available on request from the corresponding author upon reasonable request.

Declarations

Competing Interests

The authors declare no competing financial interests.

Received: 7 September 2022 Revised: 26 April 2024 Accepted: 17 May 2024

Published online: 15 July 2024

References

- [1] V Giurgiutiu. *Structural health monitoring of aerospace composites*. London: Academic Press, 2015.
- [2] S Abrate. *Impact engineering of composite structures*. Vienna: Springer Science & Business Media, 2011.
- [3] Y Sun, Z B Cai, S B Wu, et al. Effect of cycling low velocity impact on mechanical and wear properties of CFRP laminate composites. *Chinese Journal of Mechanical Engineering*, 2018, 31: 112.
- [4] M G R Sause, E Jasiūnienė. *Structural health monitoring damage detection systems for aerospace*. Cham: Springer Nature, 2021.
- [5] L Cao, J Liu, C Lu, et al. Efficient inverse method for structural identification considering modeling and response uncertainties. *Chinese Journal of Mechanical Engineering*, 2022, 35: 75.
- [6] H Inoue, J J Harrigan, S R Reid. Review of inverse analysis for indirect measurement of impact force. *Applied Mechanics Reviews*, 2001, 54(6): 503-524.
- [7] X Wang, D Guyomar, K Yuse, et al. Impact force detection using an energy flow estimator with piezoelectric sensors. *Frontiers of Mechanical Engineering in China*, 2010, 5: 194-203.
- [8] E Jacquelin, A Bennani, P Hamelin. Force reconstruction: Analysis and regularization of a deconvolution problem. *Journal of Sound and Vibration*, 2003, 265(1): 81-107.
- [9] A Thite, D Thompson. The quantification of structure-borne transmission paths by inverse methods. Part 1: Improved singular value rejection methods. *Journal of Sound and Vibration*, 2003, 264(2): 411-431.
- [10] H Tran, H Inoue. Development of wavelet deconvolution technique for impact force reconstruction: Application to reconstruction of impact force acting on a load-cell. *International Journal of Impact Engineering*, 2018, 122: 137-147.
- [11] E Zhang, J Antoni, P Feissel. Bayesian force reconstruction with an uncertain model. *Journal of Sound and Vibration*, 2012, 331(4): 798-814.
- [12] Q Li, Q Lu. Time domain force identification based on adaptive ℓ_q regularization. *Journal of Vibration and Control*, 2018, 24(23): 5610-5626.
- [13] B Qiu, M Zhang, Y Xie, et al. Localisation of unknown impact loads on a steel plate using a pattern recognition method combined with the similarity metric via structural stress responses in the time domain. *Mechanical Systems and Signal Processing*, 2019, 128: 429-445.
- [14] G Yan, H Sun, O Büyükköztürk. Impact load identification for composite structures using Bayesian regularization and unscented Kalman filter. *Structural Control and Health Monitoring*, 2017, 24(5): e1910.
- [15] S Khoo, Z Ismail, K Kong, et al. Impact force identification with pseudo-inverse method on a lightweight structure for under-determined, even-determined and over-determined cases. *International Journal of Impact Engineering*, 2014, 63: 52-62.
- [16] A Rezayat, V Nassiri, B De Pauw, et al. Identification of dynamic forces using group-sparsity in frequency domain. *Mechanical Systems and Signal Processing*, 2016, 70: 756-768.
- [17] D Ginsberg, C P Fritzen. Impact identification and localization using a sample-force-dictionary-general theory and its applications to beam structures. *Structural Monitoring and Maintenance*, 2016, 3(3): 195-214.
- [18] B Qiao, X Zhang, J Gao, et al. Sparse deconvolution for the large-scale ill-posed inverse problem of impact force reconstruction. *Mechanical Systems and Signal Processing*, 2017, 83: 93-115.
- [19] Z Yang, D Gjorgjević, J Long, et al. Sparse autoencoder-based multi-head deep neural networks for machinery fault diagnostics with detection of novelties. *Chinese Journal of Mechanical Engineering*, 2021, 34: 54.
- [20] Z Zhang, W Huang, Y Liao, et al. Bearing fault diagnosis via generalized logarithm sparse regularization. *Mechanical Systems and Signal Processing*, 2022, 167: 1-17.
- [21] X Sun, L Lin, S Jin. Resolution enhancement in ultrasonic TOFD imaging by combining sparse deconvolution and synthetic aperture focusing technique (Sparse-SAFT). *Chinese Journal of Mechanical Engineering*, 2022, 35: 94.
- [22] J Liu, B Qiao, Y Chen, et al. Impact force reconstruction and localization using nonconvex overlapping group sparsity. *Mechanical Systems and Signal Processing*, 2022, 162: 1-19.
- [23] C Pan, L Yu. Identification of external forces via truncated response sparse decomposition under unknown initial conditions. *Advances in Structural Engineering*, 2019, 22(15): 3161-3175.
- [24] J Liu, K Li. Sparse identification of time-space coupled distributed dynamic load. *Mechanical Systems and Signal Processing*, 2021, 148: 1-20.
- [25] B Qiao, J Liu, J Liu, et al. An enhanced sparse regularization method for impact force identification. *Mechanical Systems and Signal Processing*, 2019, 126: 341-367.
- [26] B Qiao, Z Mao, J Liu, et al. Group sparse regularization for impact force identification in time domain. *Journal of Sound and Vibration*, 2019, 445: 44-63.
- [27] R Chartrand. Exact reconstruction of sparse signals via nonconvex minimization. *IEEE Signal Processing Letters*, 2007, 14(10): 707-710.
- [28] W Zuo, D Meng, L Zhang, et al. A generalized iterated shrinkage algorithm for non-convex sparse coding. *Proceedings of the IEEE International Conference on Computer Vision*, Washington, USA, December 1-8, 2013: 217-224.
- [29] Z Zhang, W Huang, J Wang, et al. Morphological component analysis under non-convex smoothing penalty framework for gearbox fault diagnosis. *ISA Transactions*, 2023, 143: 525-535.
- [30] J Liu, B Qiao, W He, et al. Impact force identification via sparse regularization with generalized minimax-concave penalty. *Journal of Sound and Vibration*, 2020, 484: 1-15.
- [31] M Aucejo, O De Smet. Multi-parameter multiplicative regularization: an application to force reconstruction problems. *Journal of Sound and Vibration*, 2020, 469: 1-15.
- [32] B Qiao, C Ao, Z Mao, et al. Non-convex sparse regularization for impact force identification. *Journal of Sound and Vibration*, 2020, 477: 1-20.
- [33] M A Figueiredo, J M Bioucas-Dias, R D Nowak. Majorization-minimization algorithms for wavelet-based image restoration. *IEEE Transactions on Image Processing*, 2007, 16(12): 2980-2991.
- [34] S Boyd, N Parikh, E Chu. *Distributed optimization and statistical learning via the alternating direction method of multipliers*. Hanover: Now Publishers, 2011.

- [35] Z Xu, X Chang, F Xu, et al. $L_{1/2}$ regularization: A thresholding representation theory and a fast solver. *IEEE Transactions on Neural Networks and Learning Systems*, 2012, 23(7): 1013–1027.
- [36] Y C Eldar. Generalized SURE for exponential families: Applications to regularization. *IEEE Transactions on Signal Processing*, 2008, 57(2): 471–481.
- [37] B Qiao, X Zhang, J Gao, et al. Impact-force sparse reconstruction from highly incomplete and inaccurate measurements. *Journal of Sound and Vibration*, 2016, 376: 72–94.
- [38] T Blumensath, M E Davies. Iterative thresholding for sparse approximations. *Journal of Fourier analysis and Applications*, 2008, 14: 629–654.
- [39] Y Wang, W Yin, J Zeng. Global convergence of admm in nonconvex nonsmooth optimization. *Journal of Scientific Computing*, 2019, 78: 29–63.
- [40] P L Combettes, J C Pesquet. Proximal splitting methods in signal processing. *Fixed-point Algorithms for Inverse Problems in Science and Engineering*, 2011: 185–212.
- [41] I Daubechies, M DeFrise, C De Mol. An iterative thresholding algorithm for linear inverse problems with a sparsity constraint. *Communications on Pure and Applied Mathematics: A Journal Issued by the Courant Institute of Mathematical Sciences*, 2004, 57(11): 1413–1457.
- [42] W Cao, J Sun, Z Xu. Fast image deconvolution using closed-form thresholding formulas of L_q ($q = 1/2, 2/3$) regularization. *Journal of Visual Communication and Image Representation*, 2013, 24(1): 31–41.
- [43] I W Selesnick, I Bayram. Sparse signal estimation by maximally sparse convex optimization. *IEEE Transactions on Signal Processing*, 2014, 62(5): 1078–1092.
- [44] J Eckstein, D P Bertsekas. On the Douglas—Rachford splitting method and the proximal point algorithm for maximal monotone operators. *Mathematical Programming*, 1992, 55: 293–318.
- [45] B He, H Yang, S Wang. Alternating direction method with self-adaptive penalty parameters for monotone variational inequalities. *Journal of Optimization Theory and Applications*, 2000, 106: 337–356.
- [46] S Ramani, T Blu, M Unser. Monte-Carlo SURE: A black-box optimization of regularization parameters for general denoising algorithms. *IEEE Transactions on Image Processing*, 2008, 17(9): 1540–1554.
- [47] D L Donoho. De-noising by soft-thresholding. *IEEE Transactions on Information Theory*, 1995, 41(3): 613–627.
- [48] B An, S Wang, R Yan, et al. Adaptive robust noise modeling of sparse representation for bearing fault diagnosis. *IEEE Transactions on Instrumentation and Measurement*, 2020, 70: 1–12.

Xuefeng Chen is currently a professor at *School of Mechanical Engineering, Xi'an Jiaotong University, China*. He received his PhD degree in Engineering from *Xi'an Jiaotong University*. His research field mainly focuses on mechanical fault diagnosis.

Yanan Wang is currently an assistant professor at *School of Mechanical Engineering, Xi'an Jiaotong University, China*. She graduated with a PhD from the *University of Southampton, USA* and worked as a postdoctoral fellow at the *Rolls-Royce UTC in Propulsion Systems Noise*. She mainly studies dynamic inverse problems and aeroacoustic fault diagnosis.

Lin Chen is currently a master candidate at *School of Mechanical Engineering, Xi'an Jiaotong University, China*. She focuses her research on impact force identification of composite structures.

Junjiang Liu is currently a doctor candidate at *School of Mechanical Engineering, Xi'an Jiaotong University, China*. His main research is on solving dynamic inverse problems.

Baijie Qiao is currently a professor at *School of Mechanical Engineering, Xi'an Jiaotong University, China*. He received his PhD degree from *Xi'an Jiaotong University* and was awarded the top young A-level talent of *Xi'an Jiaotong University*. He mainly studies dynamic inverse problems and blade fault diagnosis.

Weifeng He is currently a professor at *School of Mechanical Engineering, Xi'an Jiaotong University, China*, focusing on laser manufacturing and remanufacturing.